



Lead–carbon hybrid ultracapacitors fabricated by using sulfur, nitrogen-doped reduced graphene oxide as anode material derived from spent lithium-ion batteries

Sadananda Muduli¹ · Y. Kaliprasad² · Surendra K. Martha¹

Received: 2 May 2022 / Revised: 9 May 2022 / Accepted: 11 May 2022 / Published online: 24 May 2022
© The Author(s), under exclusive licence to Springer-Verlag GmbH Germany, part of Springer Nature 2022

Abstract

The electrochemical-grade natural graphite flake prices are increasing day by day. Reusing and recycling graphite materials from the spent lithium-ion battery (LIB) is a prospective way to overcome the issue. This report presents the synthesis of reduced graphene oxide (RGO) from spent LIB by the improved Hummers method followed by calcination at 600 °C (RGO-600). S, N-RGO-600 was prepared by doping sulfur and nitrogen with RGO-600 through hydrothermal synthesis. Assynthesized S, N-RGO-600s have sheet-like morphology having uniform heteroatom doping. S- and N-doped RGO-600 delivers 375 F g⁻¹ at 5 A g⁻¹ compared to RGO-600 of 233 F g⁻¹ and retains > 98% capacitance over 20,000 cycles. The lead–carbon hybrid ultracapacitors fabricated using in-situ activated PbO₂ as cathode and S, N-RGO-600 composite electrode as anode deliver a specific capacitance of 564 F g⁻¹ at 5 A g⁻¹ and retain 90% capacitance after 15,000 cycles. The high capacitance and stable cycle life of RGO and S, N-RGO are due to easy access of electrolyte ions through mesoporous and layered graphitic carbons with redox-active functional moieties of sulfur and nitrogen. This work illustrates an easy and scalable synthesis root for RGO and S, N-RGO.

Keywords Sulfur, Nitrogen-doped RGO · Improved Hummers method · Pseudo-capacitance · Anode material · Lead–carbon hybrid ultracapacitor · Electrochemical performance

Introduction

The radical revolution in the electric-vehicle industry and the electronic world is always raising the demand for sustainable and renewable power resources due to the diminution of fossil fuels and increasing environmental pollution [1–3]. Therefore, environmentally friendly, highly efficient, lightweight, and reliable energy storage devices are essential for the innovative electronic society [1, 2]. The lithium-ion batteries have successfully taken over the market due to their high energy density of 150–250 Wh kg⁻¹ today. But high-power density supercapacitors with reliable energy density systems are urgently needed for pulse power requirements [3,

4]. However, having low energy density (< 7 Wh kg⁻¹), the EDLC and pseudo-supercapacitors cannot meet the demand of the market [4, 5]. At the same time, the researchers are focusing on hybrid supercapacitors, as they form a bridge between supercapacitors and batteries with higher energy density than the normal supercapacitors without scarifying the cyclability and high-power density [5, 6].

The carbon-based supercapacitors are the most stable energy storage devices due to the unique and novel structural morphology (0–3 dimensions) of carbon materials [1–3, 5, 7, 8]. The lithium- and sodium-based hybrid supercapacitors have emerged due to their high operating voltage window of ~4 V, subsequently higher energy. These hybrid capacitors use nonaqueous costly electrolytes and are unsafe due to flammable electrolytes [5, 6, 9, 10]. The aqueous-based supercapacitors are safer and have better cycle life than nonaqueous systems [9, 10]. Likewise, lead–carbon hybrid ultracapacitors (Pb-C HUC) are an emerging research field as they use aqueous H₂SO₄ electrolytes, have long cycle life, and serve for surge current applications [11–14]. The Pb-C HUC uses an almost similar concept to the lead-acid battery,

✉ Surendra K. Martha
martha@chy.iith.ac.in

¹ Department of Chemistry, Indian Institute of Technology Hyderabad, Kandi, Sangareddy, Telangana 502284, India

² Nile Limited, Plot No.24 A/A, MLA Colony, Road No. 12, Banjara Hills, Hyderabad, Telangana 500034, India

but only the negative lead electrode of the lead-acid battery is replaced with a supercapacitor-based carbon electrode. Moreover, the carbon negative electrode in Pb-C HUC systems resolves the unsolved sulfation issue of lead-acid batteries that occurs at the lead negative electrode [12–13]. The charge storage in Pb-C HUC is due to the Faradaic redox process due to the PbO_2 cathode and electrical double layer (EDLC) charge storage of the carbon anode. Thus, selecting a suitable carbon material is essential for the development of Pb-C HUCs [13, 14].

The most stable and effective carbons used as electrode material for energy storage applications are graphite or graphite derivatives like graphene, graphene oxides (GO), reduced graphene oxides (RGO), and heteroatom-doped RGO. Graphite demand is growing by 10–12% per year, so also the price. As vein graphite (99.9% pure) have limited resources, they cannot fulfill the demand alone [15–19]. Flake graphite and synthetic graphite can meet the demand as electrode materials for energy storage devices, but raw material purification requires high processing costs [15, 16, 20]. Therefore, recycling and reusing flake graphite from its different waste sources, such as graphite material from LIBs, is an obvious choice to mitigate the scarcity of resources and reduce environmental pollution. Also, comparative studies reveal that Li-intercalated recycled graphite electrode delivers improved electrochemical performance than the as-synthesized graphite anode [20–24].

Reduced graphene oxide synthesized from the spent lithium-ion battery by Hummers method followed by chemical reduction achieved a specific capacitance of 112 F g^{-1} at 0.5 A g^{-1} due to easy diffusion and dislocation of electrolyte ions in the layered carbon framework. The electrodes are stable up to 20,000 cycles in $0.5 \text{ M H}_2\text{SO}_4$ electrolyte because of a high degree of reduction and surface area of RGO ($115.5 \text{ m}^2 \text{ g}^{-1}$, pore diameter $\sim 4 \text{ nm}$) [25]. Nanoporous graphene synthesized by improved Hummers method followed by wet chemical reduction delivered a specific capacitance of 264 F g^{-1} at 1 A g^{-1} and fabricated symmetric supercapacitor has 95% cycling stability after 20,000 cycles. Such improved capacitance of the nanoporous graphene is due to the unique reduction of GO by Mg/Zn metal strips that result in a high BET surface area of $1294.6 \text{ m}^2 \text{ g}^{-1}$ [28]. Furthermore, sulfur-doped rGO synthesized by microwave method shows a specific capacitance of 237.6 F g^{-1} at 0.1 A g^{-1} due to the pseudocapacitive charge storage nature of S-based functional moieties. The electrodes are stable over 10,000 cycles with 106% capacitance retention in a $1 \text{ M H}_2\text{SO}_4$ electrolyte medium because of wrinkling and folded structural morphology [30]. A high percentage (6.8–8%) of N doped in graphene sheets by the carboxylation method shows a specific capacitance of 217 F g^{-1} at 0.5 A g^{-1} due to easy access of electrolyte ions and good wettability of the electrode material [33]. The involvement of pyridine and

pyridinic functional moieties favored by the presence of carboxylic groups in the few-layered N-doped graphene (~ 3 – 5) results in such capacitance [33]. Additionally, the dual doping of S and N in the graphene results in an improved specific capacitance of 344 F g^{-1} at 1 A g^{-1} in 6 M KOH electrolyte medium. The enhanced specific capacitance is due to effective disorderness and many edge defects generated by sulfur- and nitrogen-based functional moieties in the graphene structure [39]. More details of literature results of RGO, S-doped RGO, N-doped RGO, and S, N-doped RGO-based supercapacitor electrodes are presented in Supplementary Table T1 [25–41].

This work reports the synthesis of S, N-doped RGO from spent Li-ion battery anode materials. Graphene oxides were obtained by improved Hummers method followed by doping of S and N using thiourea and thermal reduction at $600 \text{ }^\circ\text{C}$. The π – π stacking of graphitic carbon layers in RGO enhances the specific capacitance compared to commercial or disordered carbons. Furthermore, doping with S and N like Lewis centers to RGO synergistically increases the charge storage behavior of S, N-RGO-600 in an aqueous electrolyte medium.

Here, we have revealed a commercially scalable and fast approach for synthesizing unique sheet-like RGOs from spent Li-ion batteries through the “improved Hummers method.” The physical interpretations of the synthesized materials were performed by microscopic (FESEM and HR-TEM) and various spectroscopic methods like Raman, XPS, XRD, and BET. The S, N-doped RGO electrode delivers the capacitance of 583 F g^{-1} at 1 A g^{-1} (375 F g^{-1} at 5 A g^{-1}) and is stable over 20,000 cycles with $> 98\%$ capacitance retention. Finally, Pb-C HUC full cells were fabricated using S, N-RGO-600 as an anode, and in situ activated PbO_2 cathode in $4.5 \text{ M H}_2\text{SO}_4$ delivers a capacitance of 564 F g^{-1} at 5 A g^{-1} and retains 90% capacitance after 15,000 cycles.

Experimental

Synthesis of RGO by improved Hummers method

Spent 18,650 Li-ion cells (original capacity: $3.7 \text{ V}/2.5 \text{ Ah}$) based on LiCoO_2 cathode and graphite anode are provided by Nile Ltd. Hyderabad, India. The LIBs were discharged below 2 V and dismantled in the glovebox. The anodes were carefully separated, and carbon materials were leached out by ultrasonication in water. The obtained black mass was washed thoroughly using 1 M HCl and distilled water. Then GO was synthesized by the “improved Hummers method” [42, 43]. In detail (Fig. 1), 1 g of black mass was mixed with 120 ml concentrated H_2SO_4 and 12 ml H_3PO_4 followed by adding 6 g of KMnO_4 . The mixture was stirred at $70 \text{ }^\circ\text{C}$ for 24 h . 3 ml of H_2O_2 was then added dropwise to the cold

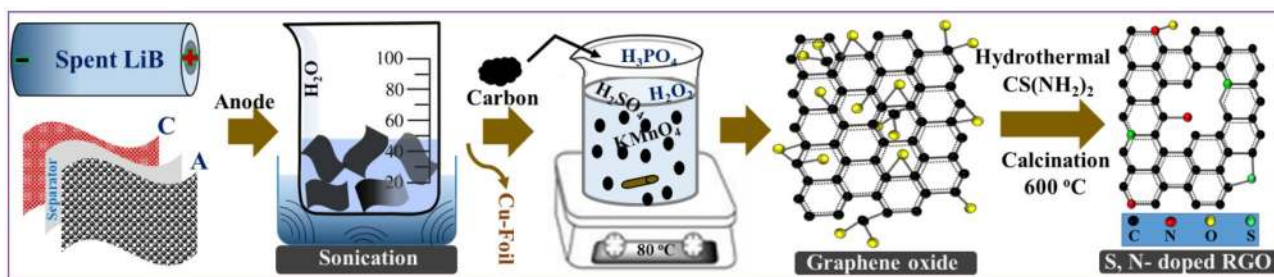


Fig. 1 Synthetic methodology for S, N-RGO-600

stirred solution, and stirring was continued for another 12 h. After that, the material was washed with 1 M HCl and water till neutralization and dried (labeled as GO). The thermal reduction of GO was carried out at 500, 600, and 700 °C for 1 h. Subsequently, the reduced GOs were leveled as RGO-500, RGO-600, and RGO-700.

Preparation of S, N-doped RGO

As RGO-600 gives better electrochemical performance (explained later in the “Results and discussion” section), S, N heteroatoms were doped to RGO-600. First, S and N doping was done by hydrothermal treatment at 180 °C for 15 h using synthesized GO and thiourea in a weight ratio of 1:3 using a 100 ml autoclave (Fig. 1). Then the carbons were washed with distilled water and dried at 100 °C. Finally, reduction of the S, N-doped GO was carried out at 600 °C for 1 h in a tubular furnace in an argon atmosphere. The synthesized carbons were labeled as S, N-RGO-600.

Morphological and structural characterizations

The morphologies of synthesized carbons were carried out by scanning electron microscopy (JEOL JIB 4700F FIB-SEM) and transmission electron microscopy (TEM-JEOL, JEM 2100FX). Furthermore, XRD was analyzed by Rigaku SmartLab X-ray diffractometer with Cu-K α ($\lambda = 1.54 \text{ \AA}$) radiation (40 mA, 40 kV) over a 2θ range from 10 to 90°. Disorderliness of materials was examined by Raman analysis with LabRam HR800 Raman spectrometer by using Ar⁺ ion laser having 532-nm green line as the excitation source. A Micrometrics ASAP 2020 Brunauer–Emmett–Teller (BET) analyzer was used for N₂ adsorption–desorption studies to measure specific surface areas. X-ray photoelectron spectroscopy (XPS) was carried out using an Shimadzu, AXIS supra⁺ XPS instrument (Japan) with Al K α as an X-ray beam at 15 kV and 40 mA. The binding energy was calibrated vs. C1s (284.6 eV) and Origin 9.0 pro having Gaussian function used for deconvolution of XPS spectra.

Electrode preparation and cell fabrications

The anodes were prepared by coating the synthesized carbons (RGOs and S, N-RGO) on a 0.5-mm-thick graphite sheet. Prior to that, the slurry of carbons was obtained by mixing 80 wt.% active material, 10 wt.% C-black, 10 wt.% polyvinylidene difluorides in dimethylformamide solvent. After coating the slurry, the composite electrodes were dried at 90 °C for 12 h in a vacuum oven. The cathodes (PbO₂) were prepared by in situ electrochemical activation followed by drying at 60 °C for 6 h in a hot air oven; detailed explanations were given in our previous works [13, 14]. The Pb-C HUC full cells were fabricated using prepared anodes and cathodes with a geometrical area of 4 cm² (2 × 2 cm²) and an absorptive glass mat separator. For all kinds of electrochemical analysis, 4.5 M H₂SO₄ is used as an electrolyte similar to that for a lead-acid battery.

Initially, the electrochemical performance of anodes (RGOs and S, N-RGO) was studied with 1 cm² active surface area in a three-electrode set-up (with Pt counter and Hg/Hg₂SO₄ reference electrode in 0.0 to –0.6 V potential range). The hybrid Pb-C full cells were electrochemically analyzed in a voltage window of 0.6 to 2.3 V. Various electrochemical experiments like CV, GCD, C-rate, cycling stability, self-discharge, and float cycling were conducted using a multi-channel cell test system (1470E Solartron analytical, Oak Ridge, TN, USA) for both 3-electrode cell and 2-electrode full cells. The impedance studies were carried out (using 1470E coupled with an FRA model 1255, Solartron analytical, Oak Ridge, TN, USA) in a frequency range of 1 MHz to 10 mHz with an AC amplitude of 5 mV.

The specific capacitance (C_s) values of carbon composite electrodes and full cells were obtained using the following equations, respectively.

$$C_s = \frac{i\Delta t}{m\Delta V} F g^{-1} \quad (\text{half - cell})$$

$$C_s = \frac{2I_m \int V dt}{\Delta V^2} F g^{-1} \quad (\text{full cell})$$

where i and I_m are applied current and current density, m is the mass of anode active material, Δt is the discharge time, $\int V dt$ is the area under discharge curve in GCD of the full cell, and ΔV is the voltage window.

Results and discussions

Morphological investigations

The surface morphologies and structure of the carbon materials play a significant role in charge storage application. The morphologies of all reduced graphene oxide samples (RGO-500, RGO-600, RGO-700) at various magnifications are shown in Fig. 2. SEM images show the formation of the packed sheets with distinct folded structures. RGO-600 shows the formation of smaller graphite flakes with particle sizes around 8–10 μm (Fig. 2c) as compared to RGO-500 of $\sim 50 \mu\text{m}$ (Fig. 2a) and RGO-700 of $\sim 120 \mu\text{m}$ (Fig. 2e). Carbonization at 600 $^\circ\text{C}$ in Fig. 2d shows the formation of thinner carbon sheets with some surface texture compared to that of 500 $^\circ\text{C}$ and 700 $^\circ\text{C}$.

A temperature of 600 $^\circ\text{C}$ could be the optimum carbonization temperature as it facilitates better exfoliation of graphitic carbon sheets. Carbonization at 500 $^\circ\text{C}$ produces larger particles due to low carbonization temperature. Similarly, at high carbonization temperatures of 700 $^\circ\text{C}$ (Fig. 2e and f), the agglomeration of sheets leads to the formation of

larger particles compared to RGO-600. This further induces better electrochemical charge storage for RGO-600 compared to RGO-500 and RGO-700, which are discussed later in the electrochemistry part of the results and discussion. Therefore, sulfur- and nitrogen-doped reduced graphene oxides have been synthesized by hydrothermal method and carbonized at 600 $^\circ\text{C}$ (S, N-RGO-600). The physical and electrochemical characterizations are carried out and thoroughly studied for RGO-600 and S, N-RGO-600 materials only.

The RGO-600 and S, N-RGO-600 materials were analyzed by HR-TEM and elemental mapping, as shown in Fig. 3. The HR-TEM image of RGO-600 (Fig. 3a) signifies that reduction at 600 $^\circ\text{C}$ results in unique ultrathin carbon sheets having wrinkles that appear due to the folding of thin graphene sheets. The high magnification images of S, N-RGO-600 (Fig. 3b–c) further confirm the presence of small and thin stacked graphene flakes. Figure 3d and e show the elemental mapping of C, O, N, and S in S, N-RGO-600. Figure 3e illustrates the uniform distribution of S and N throughout the carbon matrix that depicts the effective insertion of Lewis centers through the hydrothermal method.

Structural analysis of RGO-600 and S, N-RGO-600

The XRD patterns of RGO-600 and S, N-RGO-600 shown in Fig. 4a indicate two diffraction peaks due to (002) and (100) graphitic planes. The graphitic (002) sharp peak indicates

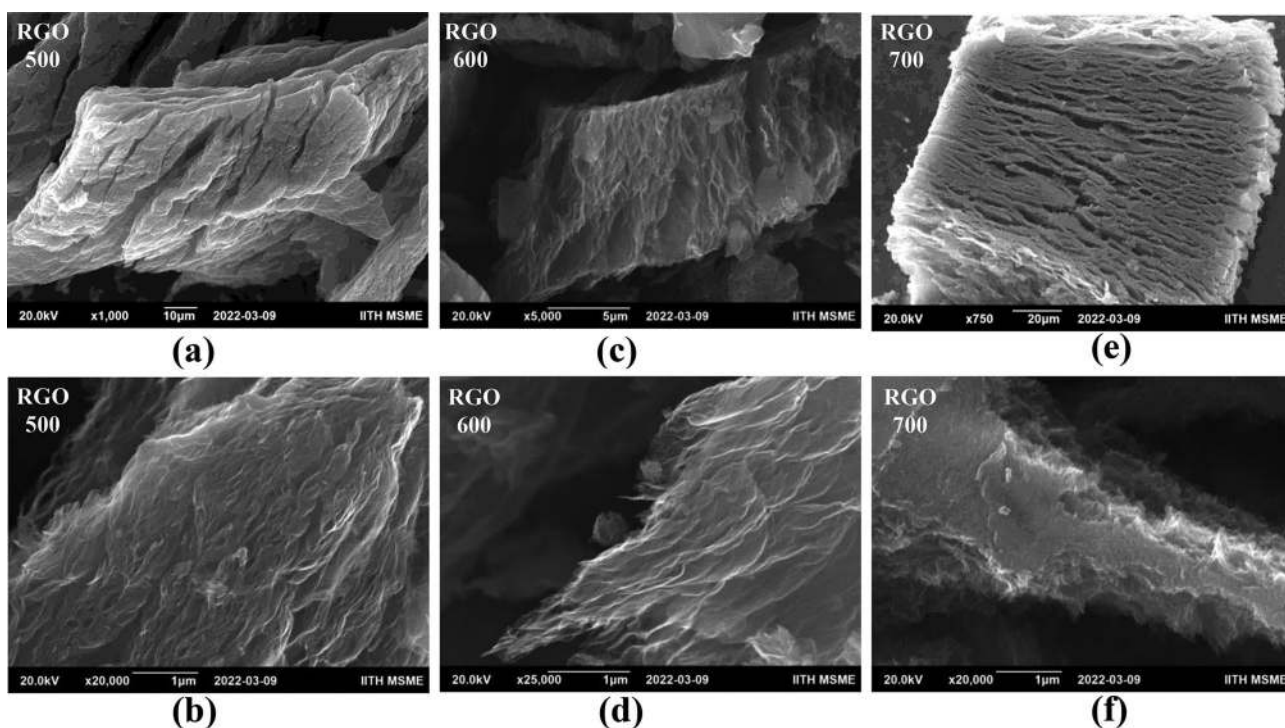


Fig. 2 SEM images: a, b RGO-500, c, d RGO-600, and e, f RGO-700 at various magnifications

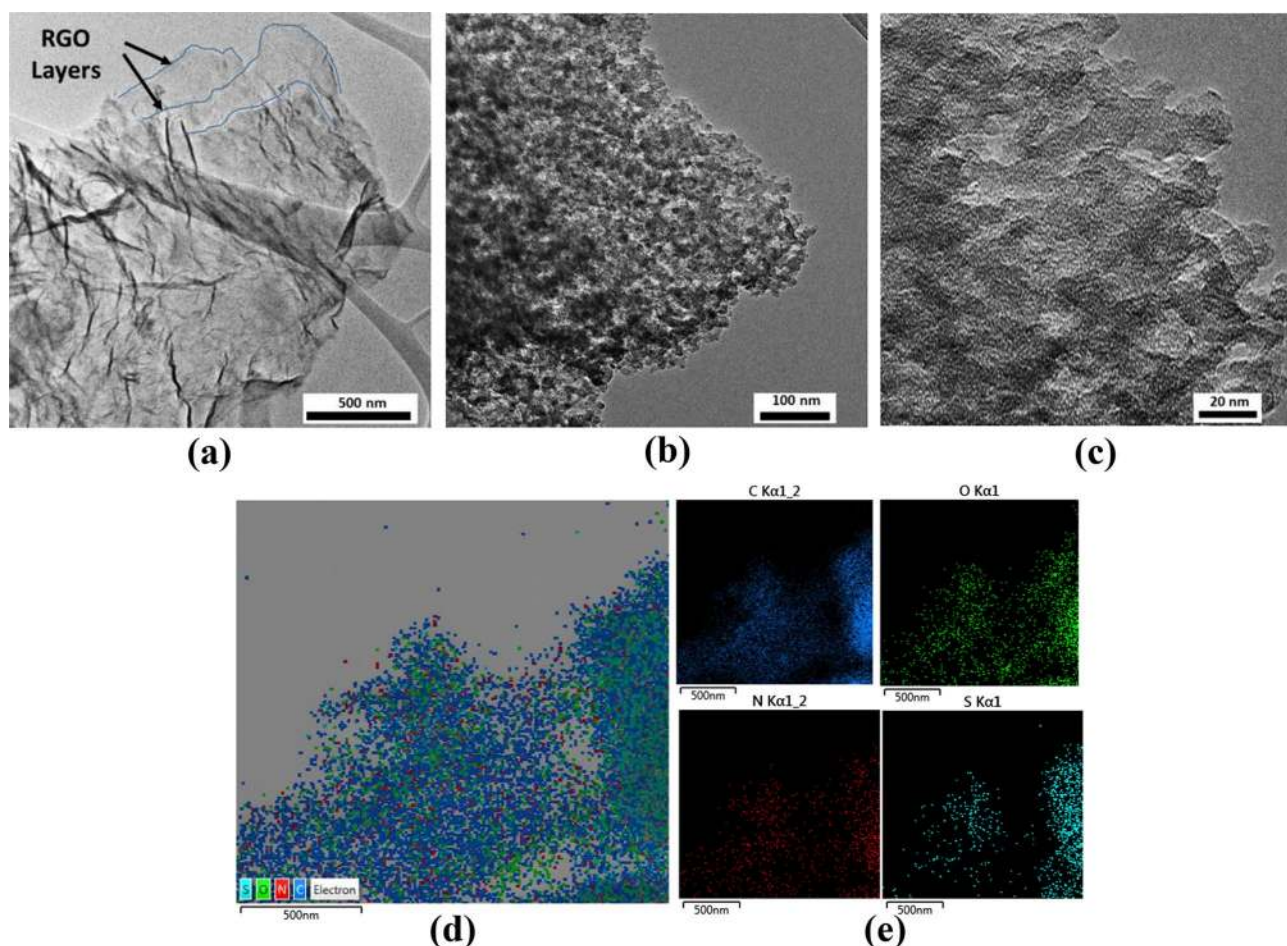


Fig. 3 TEM images: **a** RGO-600; **b**, **c** S, N-RGO-600, EDS mapping; **d** selected image for mapping of S, N-RGO-600; **e** C, O, N, and S elemental mapping (of Fig. **d**)

the higher order orientation of aromatic carbon rings in the 3D arrangement. The (100) peak is due to the layer structure in the aromatic rings [34, 39, 44]. No other metal impurities were observed in the XRD pattern indicating proper leaching of metals (basically copper and transition metals) in the carbon matrix. A little peak shift was observed for S, N-RGO than RGO-600 that confirms the enhancement in the d-spacing, i.e., 0.348 nm for RGO-600 and 0.366 nm for S, N-RGO-600. The Raman spectra analysis was carried out to understand the effect of dual doping. The spectra presented in Fig. 4b show that for RGO-600 and S, N-RGO-600, it illustrates the characteristic D and G bands. The D band is due to sp^3 carbons or defects in the graphitic domain, and G band appears due to in-plane vibration of sp^2 carbon corresponding to E_{2g} mode [30, 32, 33, 37]. The I_D/I_G ratios calculated from the spectra are 1.08 and 1.24 for RGO-600 and S, N-RGO-600, respectively. Thus, it confirms that the increase in the I_D/I_G ratio for S, N-RGO-600 is due to the dual doping of S and N heteroatom to the RGO matrix, enhancing the disorderness.

The nitrogen adsorption–desorption hysteresis loop in Fig. 4c for RGO-600 and S, N-RGO-600 shows a type IV isotherm. The specific surface areas analyzed by the Brunauer–Emmett–Teller (BET) method are 136 and 87 $m^2 g^{-1}$ for RGO-600 and S, N-RGO-600, respectively. The decrease in surface area for doped material is due to the involvement of high molecular weight sulfur and nitrogen atoms as the carbonization temperature is the same for both the materials [36, 44]. Additionally, the pore volume and average pore size measured by the Barrett–Joyner–Halenda method (Fig. 4d) are 0.18 $cm^3 g^{-1}$ and 10 nm for RGO-600 and 0.04 $cm^3 g^{-1}$ and 10 nm for S, N-RGO-600, respectively.

XPS survey scan spectrum of RGO-600 (Fig. 4e) shows C1s and O1s peaks, whereas the survey scan of S, N-RGO-600 (Fig. 4f) has additional N1s and S2s and S2p peaks that confirm the S and N heteroatoms doping to RGO-600. S, N-doped RGO-600 contains 1.6% of S and 1.0% of N. The deconvoluted spectra of S2p (Fig. 4g) show that peaks at 163.6 and 164.7 are due to $S2p_{3/2}$ and $S2p_{1/2}$ for the R-SH group, whereas peaks at 165.1 and 165.6 are due to $S2p_{3/2}$

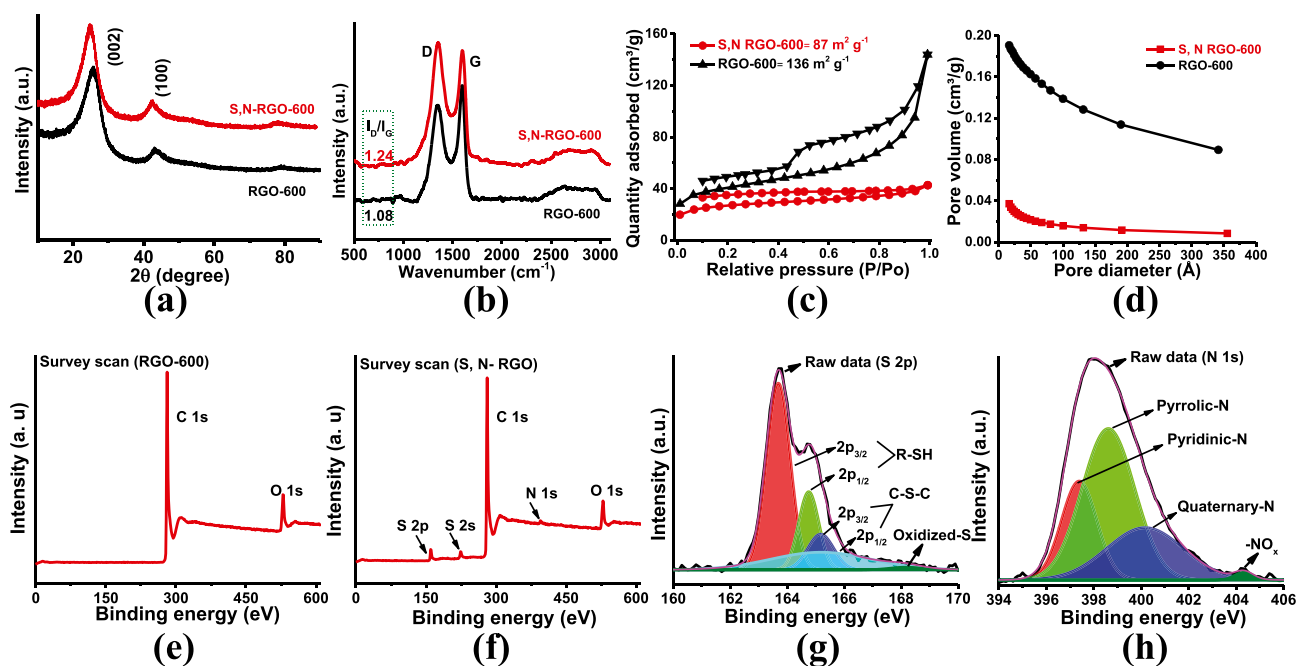


Fig. 4 Physical characterizations of RGO-600 and S, N-RGO-600: **a** XRD, **b** Raman, **c** BET, N_2 adsorption-desorption curve, **d** pore size distribution plot, **e**, **f** XPS survey scan spectrum, and **g**, **h** deconvoluted spectra of S2p and N1s of S, N-RGO-600

and $S2p_{1/2}$ for the C-S-C group. The peak at 168.1 eV arises due to oxidized sulfur moieties in the S, N-RGO-600 material. Furthermore, deconvoluted N1s peak in Fig. 4h shows that the presence of four different types of nitrogen bonds in S, N-RGO-600 is positioned at 397.3, 398.6, 400.2, and 404.2 eV, corresponding to pyrrolic, pyridinic, quaternary, and oxygenated nitrogen groups. Supplementary Figure S1a and b present the deconvoluted spectra for C1s and O1s. The high-resolution XPS scan for C1s (Fig. S1a) has the most intense peak at 283.5 eV, ascribed for C–C and C=C. The other three peaks detected at binding energies 284.4, 285.6, and 290.1 eV relate to C–N, C–S, and oxygenated carbon groups. The O1s deconvoluted spectra (Fig. S1b) show three intense peaks at 530.4, 532.4, and 534.5 eV, assigned to the COO^- , CO_3^{2-} , and absorbed oxygen groups, respectively. The oxygenated functional groups are favorable for the adsorption of the electrolyte ions, which improves the charge storage property of S, N-RGO-600. Investigation of the XPS survey scan and deconvoluted spectra analysis confirms the effective doping of the sulfur and nitrogen in the RGO [37–39, 41].

Electrochemical characterizations of composite electrodes

The charge storage phenomena of the RGO composite electrodes were examined by the GCD, CV, and EIS. The GCD plot in Fig. 5a at 1 A g^{-1} exhibits triangular asymmetric charge–discharge profiles that depict

pseudocapacitive charge storage behavior of all composite electrodes. RGO-600 material delivers more capacitance (416 F g^{-1}) than RGO-500 (358 F g^{-1}) and RGO-700 (291 F g^{-1}). S, N doping to RGO-600 further enhances the capacitance, delivering 583 F g^{-1} at 1 A g^{-1} , even though BET surface area is comparatively higher for RGO-600. This signifies nitrogen and sulfur doping to RGO-600 is an effective strategy for enhancing the charge storage property. The galvanostatic charge–discharge profiles of S, N-RGO-600 are shown in Fig. 5b–c. The specific capacitance obtained at current densities of 0.5, 1, 2, 3, 5, 7, and 10 A g^{-1} is 666, 583, 500, 435, 375, 326, and 286 F g^{-1} , respectively. As the current density increases from 0.5 to 10 A g^{-1} , charge–discharge curves convert to a symmetrical triangular shape due to fast kinetics. Also, no voltage drop (IR) occurs, indicating good stability of electrodes. At low current density, the electrolyte ions (H^+ , HSO_4^-) easily enter the interior of the electrode, improving the utilization of electrochemically active areas and thereby increasing specific capacitance. The marginal pseudocapacitive behavior is due to the functional groups and protonation in sulfuric acid solution. At high current density, electrolyte ions cannot enter the interior electrode, absorbs only on the surface of the electrode, and exhibits EDLC-type behavior [45–50]. The charge storage study (Fig. 5d) of all the composite electrodes has been carried out at various current densities between 0.5 and 10 A g^{-1} . The calculated specific capacitance values are presented in Supplementary Table T2. The capacitance values of

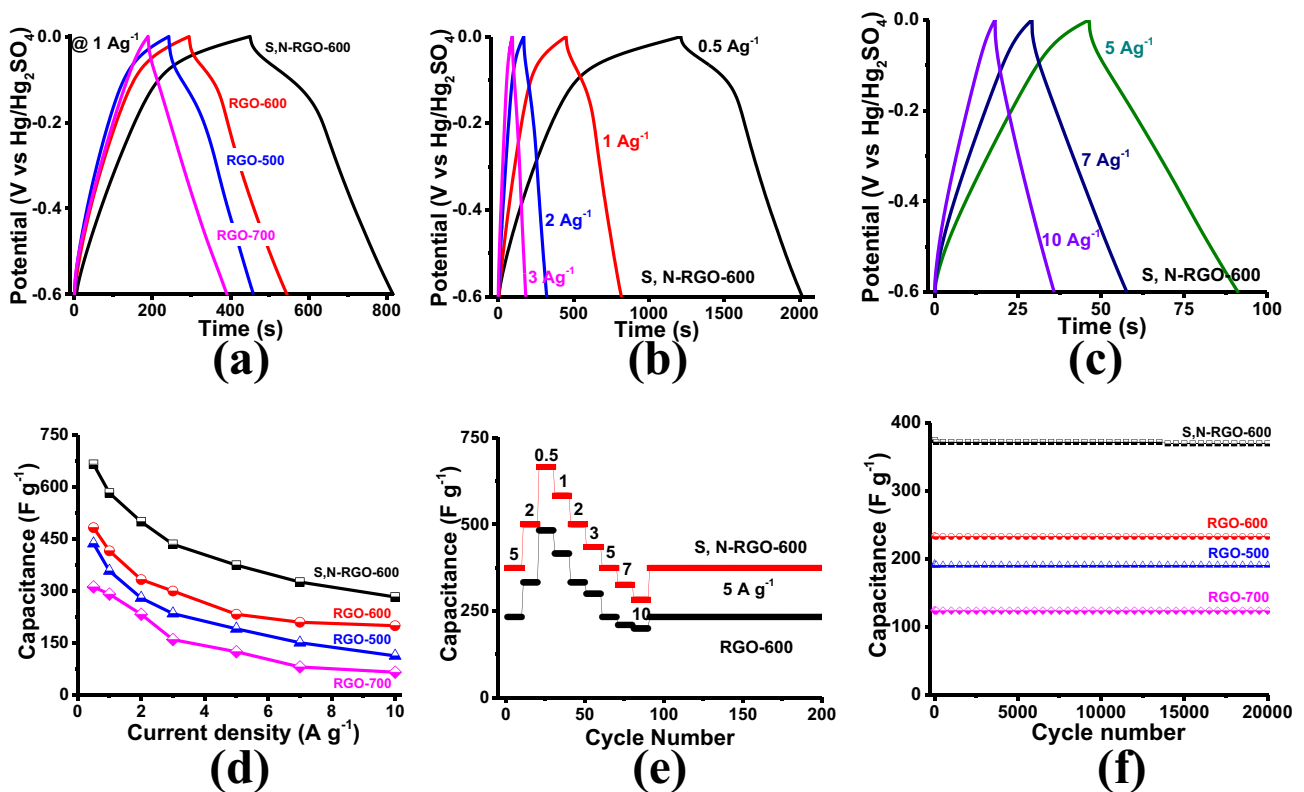


Fig. 5 Electrochemical characterizations: **a** GCD plot at 1 A g^{-1} for RGO-500, RGO-600, RGO-700, and S, N-RGO-600 composite electrodes; **b, c** GCD plot of S, N-RGO-600 at 0.5 – 10 A g^{-1} ; **d** specific capacitance at various current densities for RGO-500, RGO-600,

RGO-700, and S, N-RGO-600 composite electrodes; **e** specific capacitance at various current densities ($0.5, 1, 2, 3, 5, 7, 10 \text{ A g}^{-1}$) for RGO-600 and S, N-RGO-600; and **f** cycle life studies for RGO-500, RGO-600, RGO-700, and S, N-RGO-600 composite electrodes

RGO-600 are more than RGO-500 and RGO-700 composite electrodes at all current densities. Besides, S, N-RGO-600 stores more charges than RGO-600. The enhanced capacitance for S, N-RGO-600 is due to the synergistic effect of Lewis acid centers of sulfur and nitrogen in the carbon matrix and the porous-layer structure.

Specific capacitance at various current densities for RGO-600 and S, N-RGO-600 composite electrodes was evaluated by the GCD method, starting with a high current density of 5 A g^{-1} and then fluctuating the current densities as shown in Fig. 5e. Both the composite electrodes depict stable capacitance retention even after 10 A g^{-1} . S, N-RGO-600 composite electrodes deliver a nearly 30% increase in specific capacitance at all the current densities compared to RGO-600.

The cycling stability of the RGOs and S, N-RGO-600 has been studied by the continuous GCD method at 5 A g^{-1} , as shown in Fig. 5f. All the composite electrodes retain $> 98\%$ of capacitance over 20,000 cycles in an acidic $4.5 \text{ M H}_2\text{SO}_4$ electrolyte medium.

Furthermore, the diffusion kinetics of the electrodes are analyzed at various CV scan rates ($0.5, 1, 1.5, 2, 2.5, 3, 3.5, 4, 4.5, \text{ and } 5 \text{ mV s}^{-1}$) for the RGO-600 and S, N-RGO-600

electrodes, as shown in Fig. 6. Power law has been used to understand the charge storage contribution.

According to power law, scan rate (ν) and peak current (i) are related by the equation:

$$i = a\nu^b$$

$$\Rightarrow \log(i) = \log(a) + b \log(\nu)$$

where a and b are adjustable parameters, vary with scan rates, and can be estimated by using a $\log(i)$ vs. $\log(\nu)$ plot (Fig. 6b). If $b = 0.5$, the charge storage process is diffusion-controlled, and if $b = 1$, the method is a pure capacitive phenomenon [51, 52]. The b values derived from Fig. 6b and g lie in the range of 0.7 to 1.0 , which illustrates that the charge storage processes are a combination of both capacitive and diffusive types for RGO-600 and S, N-RGO-600 composite electrodes.

Furthermore, to examine the percentage of capacitive and diffusion-controlled charge storage at any specific scan rate, “Trasatti method” has been used. It states the total current ($i(\nu)$) at any particular potential is the sum of capacitive ($S_1\nu$) and diffusion current ($S_2\nu^{1/2}$) given by:

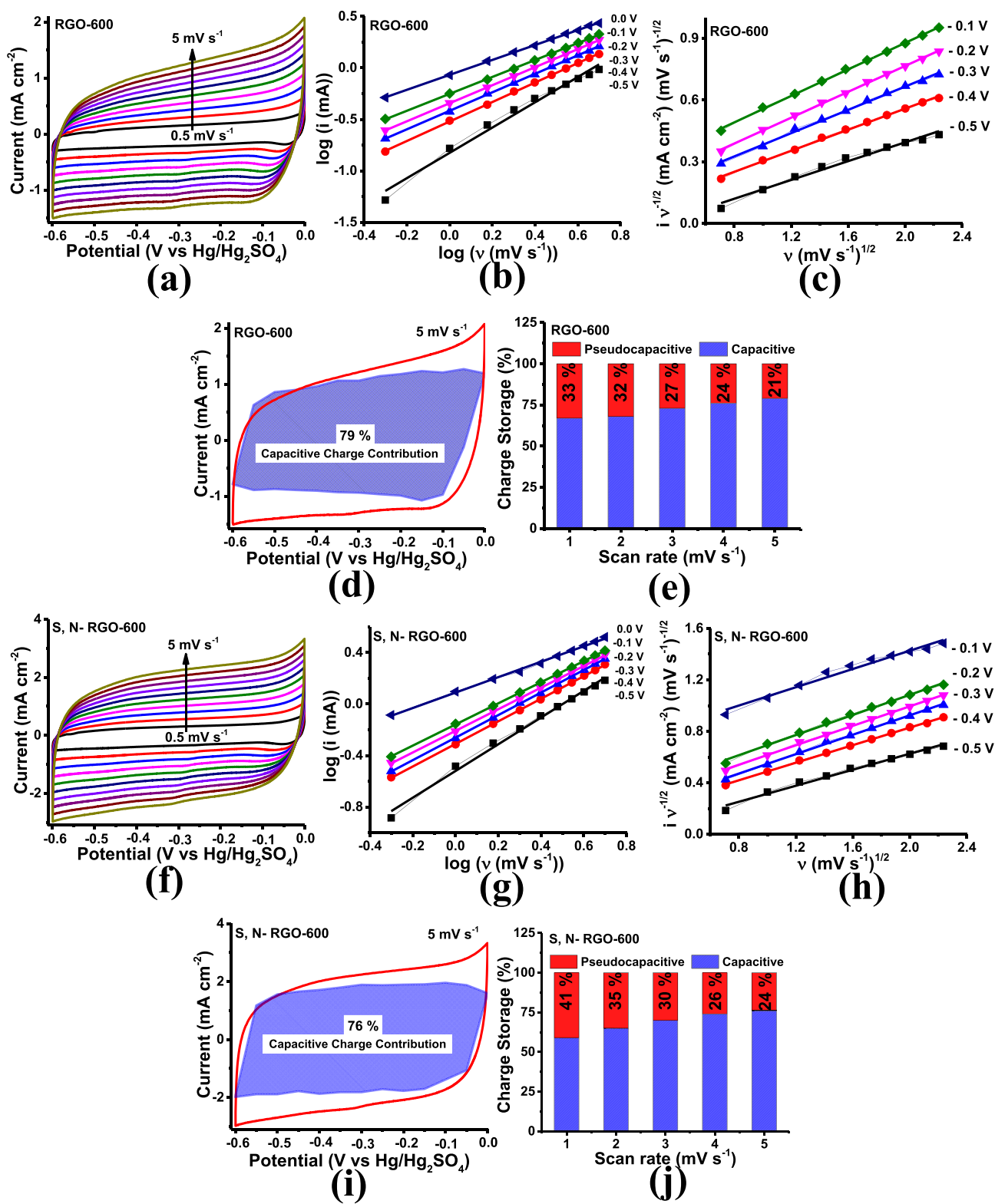


Fig. 6 Study of capacitive and pseudocapacitive charge storage percentage; RGO-600 and S, N-RGO-600. **a, f** CV at various scan rates (0.5 to 5 mV s^{-1}); **b, g** $\log(i)$ vs. $\log(v)$ plot; **c, h** $v^{1/2}$ vs. $i v^{-1/2}$ plot; **d,**

i capacitive charge storage area at 5 mV s^{-1} ; **e, j** capacitive and pseudocapacitive charge storage percentage for different scan rates

$$i(v) = S_1 v + S_2 v^{1/2}$$

$$\Rightarrow i(v)/v^{1/2} = S_1 v^{1/2} + S_2$$

The S_1 and S_2 values are adjustable parameters and can be evaluated from the plot of $i(v)/v^{1/2}$ vs. $v^{1/2}$, as shown in Fig. 6c and h. The capacitive current contribution was calculated using the S_1 and S_2 values, and the corresponding capacitive charge storage contribution curve was plotted [14, 51, 52]. Figure 6d and i depict the capacitive charge storage contribution curve at 5 mV s^{-1} , and both the capacitive and pseudocapacitive (diffusion-controlled redox reaction) charge storage percentages are illustrated in Fig. 6e and j for various scan rates. Pseudocapacitive charge storage property is higher at low scan rates due to slow kinetics related to the H^+ ion diffusion. On the other hand, the capacitive charge storage is more at high scan rate due to fast kinetics related to the adsorption of electrolyte ions at the surface of the electrode. At 5 mV s^{-1} , S, N-RGO-600 and RGO-600 show 24% and 21% pseudocapacitive type of charge storage. Heteroatom dopings improved the electrochemical performance of S, N-RGO-600 composite electrodes.

Electrochemical performance of Pb-C HUCs

Lead-carbon hybrid ultracapacitors have emerged to solve the sulfation issue of lead-acid batteries by replacing the lead anode with a supercapacitor-based carbon electrode. The Pb-C HUCs can have fast charge-discharge cycles and are essential for start-stop, electric vehicles, and high surge current applications. The electrochemistry of the cathode remains the same, but the electrode architecture is changed by aiming to keep low PbO_2 mass loading to balance with mass loading of supercapacitor carbon anode. In this work, the Pb-C HUC is fabricated by using an in situ activated PbO_2 cathode and S, N-RGO-600 composite electrode as anode in same lead-acid battery electrolyte ($4.5 \text{ M H}_2\text{SO}_4$). The CV scan at 0.5 and 1 mV s^{-1} (Fig. 7a) illustrates the Pb-C cell can operate in the voltage range between 0.6 and 2.3 V . The redox behavior of the PbO_2 cathode by CV curve at 2 mV s^{-1} is shown in Supplementary Fig. S2 [13, 14]. The GCD curves (Fig. 7b–c) for the full cell at various applied current densities ($1, 2, 3, 5, 7,$ and 10 A g^{-1}) are neither triangular nor symmetrical, indicating the pseudocapacitive behavior of a hybrid ultracapacitor. Furthermore, different slopes are observed in asymmetric GCD profiles, suggesting the involvement of redox reaction occurs at the PbO_2 positive electrode and EDLC along with the pseudocapacitive charge storage process at the negative carbon (S, N-RGO-600) electrode. The Pb-C HUC delivers a specific capacitance of $754, 681, 655, 564, 514,$ and 456 F g^{-1} at current densities of $1, 2, 3, 5, 7,$ and 10 A g^{-1} , respectively, calculated from Fig. 7b–c.

In addition, there is no initial voltage drop indicating better charge storage behavior of Pb-C HUC.

Additionally, the feasibility of the full cell has been studied by self-discharge analysis. Capacitors have the disadvantage of high self-discharge. However, the hybrid supercapacitors have a low self-discharge due to involvement of redox reactions. The self-discharge performance has been performed on fully charged Pb-C HUC cells after 10 initial GCD cycles at 1 A g^{-1} . Figure 7d shows the cell retains 1.48 V after 5 h of OCV. A sharp decrease in the voltage during the initial 0.4 h is attributed to the partial loss of the double layer to attain the thermodynamical equilibrium stage. Furthermore, a slight decrease in voltage until 3.5 h is due to the loss of pseudocapacitive charge storage driven by surface redox-active functional moieties. Ideal capacitors require some current (I_{leakage}) to maintain the potential, which can be modeled as a resistor parallel with a capacitor. The individual particles in the electrode material act as a capacitor having its own internal resistance, and thus, these require the I_{leakage} amount of current to charge gradually [53–55]. The leakage current study was carried out by fully charging and then holding at 2.3 V for 5 h (Fig. 7e). The I_{leakage} reduced quickly during initial 1 h and stabilized in 4 h. After 5 h, the I_{leakage} value is 1.8 mA . Such low leakage current value for these Pb-C HUCs opens an opportunity for real-time application. To understand the cell feasibility to a better extent, float cycling analysis has been carried out for 150 h, as shown in Fig. 7f and g. Initially, the cell undergoes 5 GCD cycles, holds for 5 h at a maximum voltage of 2.3 V , and then again undergoes another 5 GCD cycles (Fig. 7g) and continues for 150 h of floating (excluding GCD timing). The specific capacitance was calculated from the 4th discharge curve of each set of 5 GCD cycles. The cell retains 88% of capacitance after 150 h of floating (Fig. 7f), which illustrates the good stability of the cell. The cycle stability of Pb-C HUC cells was performed at a high current density of 5 A g^{-1} for 15,000 cycles, as shown in Fig. 7h. The Pb-C HUCs are very stable and retain 90% capacitance after 15,000 cycles. The stable cycling is due to easy access of electrolyte ions through mesoporous and layered graphitic carbons with redox-active functional moieties [25]. In addition, impedance studies were also conducted during different stages of the cycling stability study. The cell impedances were analyzed after the 1st, 9000th, and 15000th cycles, as presented in Fig. 7i. The low-frequency region shows a slight reduction in capacitive nature with increasing continuous GCD cycles for 15,000 cycles. The high-frequency part of the impedance plot explains a minor increase in the solution resistance (R_s) during 15,000 cycles. R_s values after 1st, 9000th, and 15000th cycles are $1.3, 3.2,$ and 3.7 ohms , respectively. The low R_s value and low-frequency curve incline towards the imaginary axis illustrate the Pb-C HUC cell's excellent supercapacitive nature. Finally, as

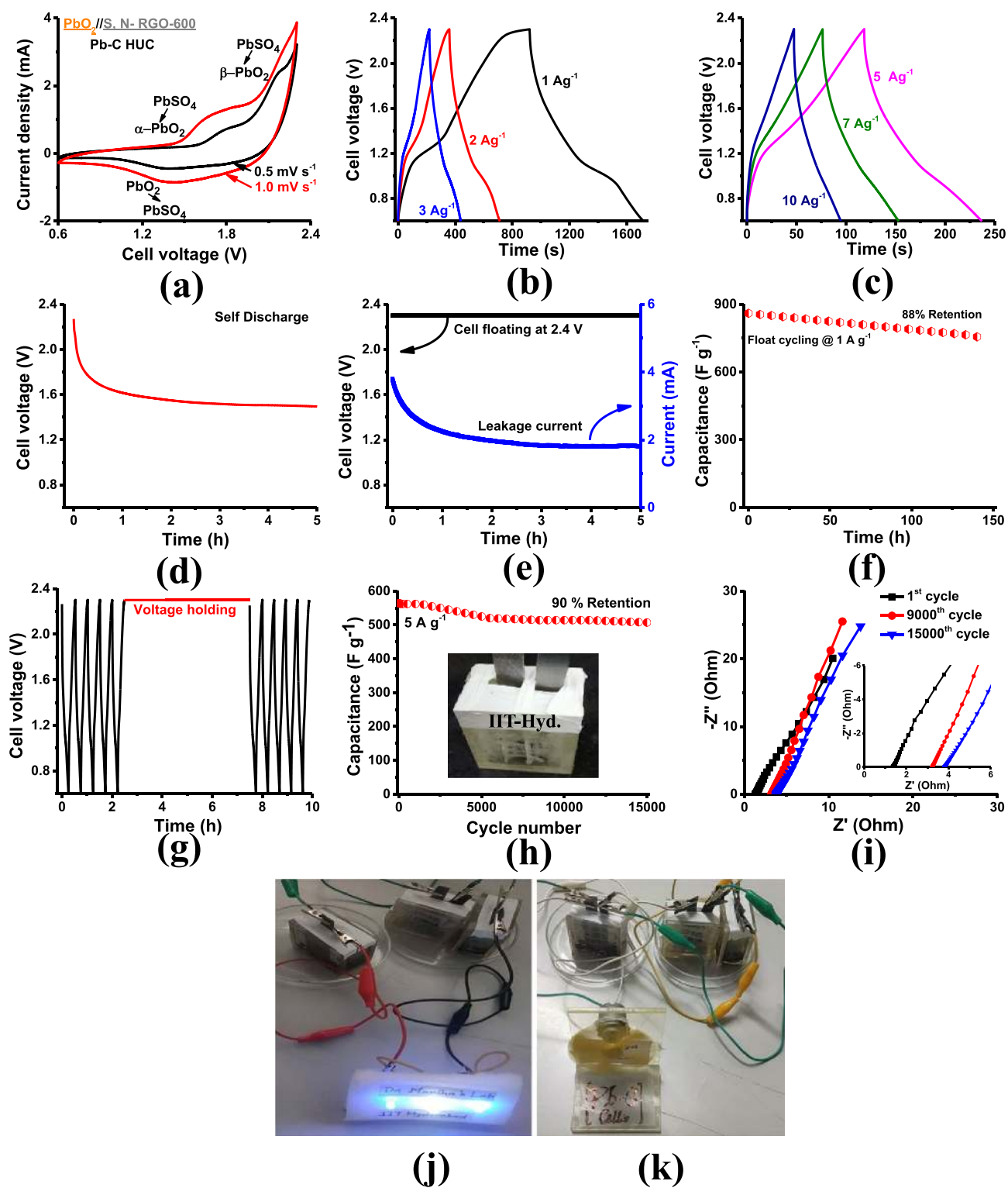


Fig. 7 Electrochemical study of Pb-C HUC full cells, **a** CV at 0.5 and 1 mVs⁻¹, **b**, **c** GCD profile at various current densities, **d** self-discharge study, **e** leakage current analysis, **f**, **g** float cycling study,

h cycle life study, **i** impedance plot (insert, high-frequency region of Fig. **i**), **j**, **k** illumination of LED light by series connection and running a toy fan parallel connection of three cells

shown in Fig. 7j and k, three LED lights were illuminated for more than 10 min by connecting three Pb-C HUC cells in series, and a toy fan was run by connecting three Pb-C HUC cells in parallel. The charge–discharge profiles at 1 A g^{-1} of three Pb-C HUC cells in series and parallel are presented in Supplementary Figure S3.

Overall, S, N-RGO-600 composite electrodes deliver maximum capacitance in both three-electrode half-cell and two electrode hybrid supercapacitors. The heteroatom-doped composite electrodes have good cycle life and C-rate performance with better capacitance. This is due to the formation of layered carbon sheets like morphology with some surface texture and an optimum carbonization temperature that enhances active areas of S, N-RGO-600. The substantial rise in specific capacitance is due to the considerable improvement in the disorderness of S, N-RGO-600 and d-spacing of the graphitic layers, which leads to better insertion/de-insertion of hydrogen ions followed by adsorption/desorption in the layered graphitic carbon matrix. Also, the participation of redox behavior of the heteroatom-based functional groups along with oxygenated functional moieties in $4.5 \text{ M H}_2\text{SO}_4$ electrolyte synergistically enhances specific capacitance.

Conclusions

In conclusion, reduced graphene oxides were synthesized from spent Li-ion batteries by a scalable and simple improved Hummers method. Effectively, sulfur and nitrogen doping to RGO has been driven by a one-step hydrothermal method. SEM confirmed the formation of surface texture carbon sheets by carbonization of GO at $600 \text{ }^\circ\text{C}$. XPS and TEM characterizations endorsed the efficient and uniform doping of S and N to the RGO-600 carbon matrix. The RGO-600 electrodes deliver up to 233 F g^{-1} at 5 A g^{-1} , but S and N doping increases the capacitance up to 375 F g^{-1} at 5 A g^{-1} . Both RGO-600 and S, N-RGO-600 retain $> 98\%$ capacitance over 20,000 cycles in 4.5 M sulfuric acid electrolyte medium. At 5 mV s^{-1} , S, N-RGO-600 and RGO-600 show 24% and 21% pseudocapacitive type of charge storage.

The lead–carbon hybrid ultracapacitors fabricated using in situ activated PbO_2 as cathode and S, N-RGO-600 composite electrode as anode deliver a specific capacitance of 564 F g^{-1} at 5 A g^{-1} and retain 90% capacitance after 15,000 cycles. The high capacitance and stable cycle life of RGO and S, N-RGO are due to easy access of electrolyte ions through mesoporous and layered graphitic carbons with redox-active functional moieties of sulfur and nitrogen.

Supplementary information The online version contains supplementary material available at <https://doi.org/10.1007/s10008-022-05188-w>.

Acknowledgements Sadananda Muduli acknowledges Ministry of Education, Govt. of India, for fellowship. We are happy to acknowledge MECSP-2K17 program of DST-IISc Energy Storage Platform on Supercapacitors and Power Dense Devices under the grant no. DST/TMD/MECSP/2K17/20 for financial support to this project work. Dr. P Vijayakumar from the Department of Chemistry at IIT Hyderabad is gratefully acknowledged here for help in XPS characterizations.

Funding We acknowledge MECSP-2K17 program of DST-IISc Energy Storage Platform on Supercapacitors and Power Dense Devices under the grant no. DST/TMD/MECSP/2K17/20 for financial support to this project work.

Declarations

Conflict of interest The authors declare no competing interests.

References

1. Qian W, Jun Y, Zhuangjun F (2016) Carbon materials for high volumetric performance supercapacitors: design, progress, challenges and opportunities. *Energy Environ Sci* 9:729–762. <https://doi.org/10.1039/C5EE03109E>
2. Fan Z, Tengfei Z, Xi Y, Long Z, Kai L, Yi H (2013) Yongsheng C. A high-performance supercapacitor-battery hybrid energy storage device based on graphene-enhanced electrode materials with ultrahigh energy density. *Energy Environ Sci* 6:1623. <https://doi.org/10.1039/c3ee40509e>.
3. Zhibin L, Jintao Z, Li LZ, Nanjundan AK, Zhao XS (2016) Functionalization of chemically derived graphene for improving its electrocapacitive energy storage properties. *Energy Environ Sci* 9:1891–1930. <https://doi.org/10.1039/C6EE00158K>
4. Tao M, Hongxing Y, Lin L (2015) Development of hybrid battery–supercapacitor energy storage for remote area renewable energy systems. *Appl Energy Supercapacitors* 153:56–62. <https://doi.org/10.1016/j.apenergy.2014.12.008>
5. Aqib M, Ahamed MB, Kalim D, Jagannathan T (2019) A review on recent advances in hybrid supercapacitors: design, fabrication and applications. *Renew Sustain Energy Rev* 101:123–145. <https://doi.org/10.1016/j.rser.2018.10.026>
6. Vlad A, Singh N, Rolland J, Melinte S, Ajayan PM, Gohy JF (2014) Hybrid supercapacitor-battery materials for fast electrochemical charge storage. *Sci Rep* 4:4315. <https://doi.org/10.1038/srep04315>
7. Xuli C, Rajib P, Liming D (2017) Carbon-based supercapacitors for efficient energy storage. *Natl Sci Rev* 4:453–489. <https://doi.org/10.1093/nsr/nwx009>
8. Ling M, Ziyang S, Dazhang Z, Liangchun L, Lihua G, Mingxian L (2020) Recent advances in carbon-based supercapacitors. *Mater Adv* 1:945–966. <https://doi.org/10.1039/D0MA00384K>
9. Lina C, Xiaowen Z, Chongyang H, Youri W, Jun C, Hongqiang Z, Junwei W, Pengchao S, Lijie C (2021) A high-energy, long cycle life aqueous hybrid supercapacitor enabled by efficient battery electrode and widened potential window. *J Alloys Compd* 877:160273. <https://doi.org/10.1016/j.jallcom.2021.160273>
10. Ji-Chi L, Zi-Hang H, Tian YM (2020) aqueous supercapacitor with ultrahigh voltage window beyond 2.0 Volt. *Small Struct* 1:2000020. <https://doi.org/10.1002/ssr.202000020>.
11. Nengfei Y, Go L, Shuhong Z, Zidong W (2009) Electrodeposited PbO_2 thin film as positive electrode in PbO_2/AC hybrid capacitor. *Electrochim Acta* 54:3835–3841. <https://doi.org/10.1016/j.electacta.2009.01.086>

12. Anjan B, Ravikumar MK, Jalajakshi A, Suresh KP, Gaffoor SA, Shukla AK (2012) Substrate integrated lead-carbon hybrid ultracapacitor with flooded, absorbent glass mat and silica-gel electrolyte configurations. *J Chem Sci* 124:747–762. <https://doi.org/10.1007/s12039-012-0273-x>
13. Sadananda M, Vangapally N, Surendra KM (2020) Boron, nitrogen-doped porous carbon derived from biowaste orange peel as negative electrode material for lead-carbon hybrid ultracapacitors. *J Electrochem Soc* 167:090512. <https://doi.org/10.1149/1945-7111/ab829f>
14. Sadananda M, Vangapally N, Subir KP, Subrata D, Surendra KM (2021) Polypyrrole-MoS₂ nanopetals as efficient anode material for lead-based hybrid ultracapacitors. *J Electrochem Soc* 168:050523. <https://doi.org/10.1149/1945-7111/abfd77>
15. Moradi B, Gerardine GB (2016) Recycling of graphite anodes for the next generation of lithium-ion batteries. *J Appl Electrochem* 46:123–148. <https://doi.org/10.1007/s10800-015-0914-0>
16. Mathis W (2006) Graphite and carbon powders for electrochemical applications. *J Power Sources* 156:142–150. <https://doi.org/10.1016/j.jpowsour.2006.02.064>
17. Dissanayake CB (1981) The origin of graphite of Sri Lanka. *Organic Geochem* 3:1–7. [https://doi.org/10.1016/0146-6380\(81\)90006-1](https://doi.org/10.1016/0146-6380(81)90006-1)
18. Taylor J, Harold (2000) A graphite natural. In *Kirk-Othmer Encyclopedia of Chemical Technology*. John Wiley & Sons, Ltd. <https://doi.org/10.1002/0471238961.1401202120012512.a01>
19. Prithu M, Rakesh KG (2012) Graphite, graphene, and their polymer nanocomposites. CRC Press
20. Ohzeki K, Saito Y, Golman B, Shinohara K (2005) Shape modification of graphite particles by rotational impact blending. *Carbon* 43:1673–1679. <https://doi.org/10.1016/j.carbon.2005.02.007>
21. Ciez RE, Whitacre JF (2019) Examining different recycling processes for lithium-ion batteries. *Nat Sustain* 2:148–156. <https://doi.org/10.1038/s41893-019-0222-5>
22. Gavin H, Roberto S, Emma K, Laura D, Peter S, Rustam S, Allan W (2019) Recycling lithium-ion batteries from electric vehicles. *Nature* 575:75–86. <https://doi.org/10.1038/s41586-019-1682-5>
23. Chengjian X, Qiang D, Linda G, Mingming H, Arnold T, Bernhard S (2020) Future material demand for automotive lithium-based batteries. *Commun Mater* 1:99. <https://doi.org/10.1038/s43246-020-00095-x>
24. Yang L, Liu Y, Guangri X, Qigao F, Yuanchao L, Erqing Z, Jingjing M, Shumin F, Xiaobo L (2019) Separation and recovery of carbon powder in anodes from spent lithium-ion batteries to synthesize graphene. *Sci Rep* 9:9823. <https://doi.org/10.1038/s41598-019-46393-4>
25. Subramanian N, Sivasankara RE, Hari CB, Subrata K (2018) Environmental benign synthesis of reduced graphene oxide (RGO) from spent lithium-ion batteries (LIBs) graphite and its application in supercapacitor. *Colloids Surf A* 543:98–108. <https://doi.org/10.1016/j.colsurfa.2018.01.054>
26. Johra FT, Jung WG (2015) Hydrothermally reduced graphene oxide as a supercapacitor. *Appl Surf Sci* 357:1911–14. <https://doi.org/10.1016/j.apsusc.2015.09.128>
27. Qingguo S, Jie T, Yuexian L, Jing L, Faxiang Q, Kun Z, Jinshi Y, Lu CQ (2015) Ionic liquid modified graphene for supercapacitors with high rate capability. *Electrochim Acta* 176:1441–1446. <https://doi.org/10.1016/j.electacta.2015.07.070>
28. Senthilkumar E, Sivasankar V, Ravindra KB, Thileepkumar K, Ramya M, Sivagaami SG, Raghu S, Kalaivani R (2018) A synthesis of nanoporous graphene and their electrochemical performance in a symmetric supercapacitor. *Appl Surf Sci* 460:17–24. <https://doi.org/10.1016/j.apsusc.2017.10.221>
29. Zhuangnan L, Srinivas G, Yuchen Y, Guanjie H, Jian G, Juntao L, Yue L (2019) Exceptional supercapacitor performance from optimized oxidation of graphene-oxide. *Energy Storage Mater* 17:12–21. <https://doi.org/10.1016/j.ensm.2018.12.006>
30. Nurul HAR, Kam SL, Tan W, Siew XC, Chin HC (2021) Synergistic effect of sulfur-doped reduced graphene oxide created via microwave-assisted synthesis for supercapacitor applications. *Diam Relat Mater* 120:108696. <https://doi.org/10.1016/j.diamond.2021.108696>
31. Xu Y, Ho SP (2014) Sulfur-incorporated, porous graphene films for high performance flexible electrochemical capacitors. *Carbon* 77:59–65. <https://doi.org/10.1016/j.carbon.2014.05.002>
32. Malarkodi D, Saravanan N, Balamuralitharan B, Selvam S, Karthick SN, Prabakar K, Chang SH, Hee JK (2018) Superior one-pot synthesis of a doped graphene oxide electrode for a high-power density supercapacitor. *New J Chem* 42:11093–11101. <https://doi.org/10.1039/C8NJ01672K>
33. Bingqiao X, Ying C, Mengying Y, Xiang S, Hanwu L, Ting X, Yong Z, Yucheng W (2015) Carboxyl-assisted synthesis of nitrogen-doped graphene sheets for supercapacitor applications. *Nanoscale Res Lett* 10:332. <https://doi.org/10.1186/s11671-015-1031-z>
34. Delong L, Chaozhi Y, Miaosheng W, Yupeng Z, Chunxu P (2014) Synthesis of nitrogen doped graphene from graphene oxide within an ammonia flame for high performance supercapacitors". *RSC Adv* 4:55394–55399. <https://doi.org/10.1039/C4RA10761F>
35. Shuge D, Zhen L, Bote Z, Jianhuang Z, Hao H, Qiaobao Z, Dongchang C, Chong Q, Dai D, Meilin L (2018) A high-performance supercapacitor electrode based on N-doped porous graphene. *J Power Sources* 387:43–48. <https://doi.org/10.1016/j.jpowsour.2018.03.055>
36. Zesheng L, Bolin L, Zhisen L, Dehao L, Hongqiang W, Qingyu L (2016) One-pot construction of 3-D nitrogen-doped activated graphene-like nanosheets for high-performance supercapacitors. *Electrochim Acta* 190:378–387. <https://doi.org/10.1016/j.electacta.2015.12.210>
37. Jinghao H, Peng Z, Xiaofei W, Shouwu G (2018) Three-dimensional sulphur/nitrogen co-doped reduced graphene oxide as high-performance supercapacitor binder-free electrodes. *Appl Surf Sci* 442:575–580. <https://doi.org/10.1016/j.apsusc.2018.01.221>
38. Naresh KR, Vangapally N, Sadananda M, Venu R, Srikanth VVS, Surendra KM (2020) Microwave aided scalable synthesis of sulfur, nitrogen co-doped few-layered graphene material for high-performance supercapacitors. *Electrochim Acta* 363:137209. <https://doi.org/10.1016/j.electacta.2020.137209>
39. Ying W, Mingmei Z, Denghui P, Yuan L, Tianjiao M, Jimin X (2018) Nitrogen/sulfur co-doped graphene networks uniformly coupled N-Fe₂O₃ nanoparticles achieving enhanced supercapacitor performance". *Electrochim Acta* 266:242–253. <https://doi.org/10.1016/j.electacta.2018.02.040>
40. Riccardo B, Luca P, Roberto P, Valerio C, Alessandro M, Gian AR, Abdirisak AI, Christian D, Armando G (2017) Nitrogen and sulfur doped mesoporous carbons, prepared from templating silica, as interesting material for supercapacitors. *Chem Select* 2:7082–7090. <https://doi.org/10.1002/slct.201701404>
41. Liang C, Mengting S, Binhong H, Minjie Z, Chenxi X, Zhenguo C, Yafei K (2019) Effect of two-step doping pathway on the morphology, structure, composition, and electrochemical performance of three-dimensional N, S-codoped graphene framework. *J Mater Res* 34:1993–2002. <https://doi.org/10.1557/jmr.2019.107>
42. Lavin L, Maria d P, Amaya R, Jesus G, Luz SS, José LV (2016) Influence of different improved Hummers method modifications on the characteristics of graphite oxide in order to make a more easily scalable method. *Ind Eng Chem Res* 55:12836–12847. <https://doi.org/10.1021/acs.iecr.6b03533>
43. Daniela CM, Dmitry VK, Jacob MB, Alexander S, Zhengzong S, Alexander S, Lawrence BA, Wei L, James MT (2010) Improved synthesis of graphene oxide. *ACS Nano* 4:4806–4814. <https://doi.org/10.1021/nn1006368>

44. Tao W, Lu XW, Dong LW, Wei X, Dian ZJ (2015) Interaction between nitrogen and sulfur in co-doped graphene and synergetic effect in supercapacitor. *Sci Rep* 5:9591. <https://doi.org/10.1038/srep09591>
45. Yu LX, Qian NG (2022) Improved electrochemical performance of mesoporous carbon via N/S doping. *J Solid State Electrochem* 1013–20. <https://doi.org/10.1007/s10008-022-05145-7>
46. Dan L, Chaopeng F, Ningshuang Z, Yanling L, Haihui Z, Yafei K (2017) Porous nitrogen-doped graphene for high energy density supercapacitors in an ionic liquid Electrolyte. *J Solid State Electrochem* 21:759–766. <https://doi.org/10.1007/s10008-016-3431-0>
47. Liu HD, Zhang JL, Xu DD, Huang LH, Tan SZ, Mai WJ (2015) Easy one-step hydrothermal synthesis of nitrogen-doped reduced graphene oxide/iron oxide hybrid as efficient supercapacitor material. *J Solid State Electrochem* 19:135–144. <https://doi.org/10.1007/s10008-014-2580-2>
48. Bharathidasan P, Devaraj S, Sivakkumar SR (2020) The capacitance properties of nitrogen doped reduced graphene oxide obtained by using commercial protein powder as a nitrogen dopant. *J Solid State Electrochem* 24:1095–1103. <https://doi.org/10.1007/s10008-020-04565-7>
49. Xiaojie Z, Xiaoyan G, Zhanyu W, Minghai Z, Qinghai J, Shoubin Z, Yi H, Zhonghao R (2019) High-capacitance supercapacitor based on nitrogen-doped porous carbons-sandwiched graphene hybrid frameworks. *Ionics* 25:6017–6023. <https://doi.org/10.1007/s11581-019-03154-7>
50. Chunnian C, Wei F, Ting M, Xuwang F (2014) Fabrication of functionalized nitrogen-doped graphene for supercapacitor electrodes. *Ionics* 20:1489–1494. <https://doi.org/10.1007/s11581-014-1231-z>
51. John W, Julien P, James L, Bruce D (2007) Pseudocapacitive contributions to electrochemical energy storage in TiO₂ (anatase) nanoparticles. *J Phys Chem C* 111:14925–14931. <https://doi.org/10.1021/jp074464w>
52. Yuqi J, Jinping L (2019) Definitions of pseudocapacitive materials: a brief review. *Energy Environ Mater* 2:30–37. <https://doi.org/10.1002/eem2.12028>
53. Jari K, Suvi L, Arman D, Sampo T, Timo F, Thomas K, Anna R, Donald L (2016) Architectural modifications for flexible supercapacitor performance optimization. *Electron Mater Lett* 12:795–803. <https://doi.org/10.1007/s13391-016-6141-y>
54. Mazharul H, Qi L, Anderson DS, Volodymyr K, Per R, Peter L, Peter E (2020) Self-discharge and leakage current mitigation of neutral aqueous-based supercapacitor by means of liquid crystal additive. *J Power Sources* 453:227897. <https://doi.org/10.1016/j.jpowsour.2020.227897>
55. Quoc DN, Yi HW, Tzi YW, Ming JD, Cheng HY, Jeng KC (2016) Gravimetric/volumetric capacitances, leakage current, and gas evolution of activated carbon supercapacitors. *Electrochim Acta* 222:1153–1159. <https://doi.org/10.1016/j.electacta.2016.11.087>

Publisher's Note Springer Nature remains neutral with regard to jurisdictional claims in published maps and institutional affiliations.